

WASP-69b’s Escaping Envelope Is Confined to a Tail Extending at Least 7 R_p

Dakotah Tyler¹, Erik A. Petigura¹, Antonija Oklopčič², and Trevor J. David³¹Department of Physics and Astronomy, University of California, Los Angeles, CA 90095, USA²Anton Pannekoek Institute for Astronomy, University of Amsterdam, Science Park 904, NL-1098 XH Amsterdam, The Netherlands³Center for Computational Astrophysics, Flatiron Institute, New York, NY 10010, USA

Received 2023 May 25; revised 2023 November 13; accepted 2023 December 1; published 2024 January 9

Abstract

Studying the escaping atmospheres of highly irradiated exoplanets is critical for understanding the physical mechanisms that shape the demographics of close-in planets. A number of planetary outflows have been observed as excess H/He absorption during/after transit. Such an outflow has been observed for WASP-69b by multiple groups that disagree on the geometry and velocity structure of the outflow. Here, we report the detection of this planet’s outflow using Keck/NIRSPEC for the first time. We observed the outflow 1.28 hr after egress until the target set, demonstrating the outflow extends *at least* 5.8×10^5 km or $7.5 R_p$. This detection is significantly longer than previous observations, which report an outflow extending ~ 2.2 planet radii just 1 yr prior. The outflow is blueshifted by -23 km s⁻¹ in the planetary rest frame. We estimate a current mass-loss rate of $1 M_{\oplus}$ Gyr⁻¹. Our observations are most consistent with an outflow that is strongly sculpted by ram pressure from the stellar wind. However, potential variability in the outflow could be due to time-varying interactions with the stellar wind or differences in instrumental precision.

Unified Astronomy Thesaurus concepts: [Hot Jupiters \(753\)](#); [Exoplanet evolution \(491\)](#); [Exoplanet atmospheres \(487\)](#)

1. Introduction

The distribution of exoplanet sizes and orbital distance encodes key aspects of planet formation physics such as rocky core growth, the accretion/loss of gaseous envelopes, orbital migration, and other processes. NASA’s Kepler mission revealed that planets between the size of Earth and Neptune occur at a rate of ~ 1 per star (see, e.g., Petigura et al. 2022). In addition, there are notable “deserts” in the Kepler census. One such feature is the “hot-Neptune desert,” a lack of short-period $2\text{--}8 R_{\oplus}$ planets (Szabó & Kiss 2011). Another is the “radius gap,” in which we observe a bimodal size distribution of super-Earths and sub-Neptunes with few planets in between (1.4 and $2.0 R_{\oplus}$; Fulton et al. 2017).

One theory explains these “deserts” as a consequence of photoevaporation (see Owen & Wu 2017 and references therein), where X-ray and extreme-ultraviolet radiation (10 eV– 100 keV) heats the the upper layers of a planet’s H/He envelope, which creates a pressure gradient that drives a Parker-like outflow. Given these theories, any real-time observations of envelope loss are illuminating.

Early works such as Seager & Sasselov (2000) proposed that a transiting exoplanet with sufficiently strong absorption features (such as He I 10830 Å) in its atmosphere would be superimposed on the stellar flux passing through the planet atmosphere above the limb. The first successful outflow detection was a Ly α absorption during the transit of HD 209458b (Vidal-Madjar et al. 2003).

While Ly α presents a large absorption cross section, it cannot be observed from the ground because it is blueward of the UV cutoff of the Earth’s atmosphere. Separately, space-based observations must contend with contamination from the

interstellar medium and geocoronal emission. However, in recent years, observing the He I 10830 Å absorption line during transit has emerged as another probe of planetary outflows as it is sufficiently populated under favorable conditions (Oklopčič & Hirata 2018). Extreme-ultraviolet (EUV) ($h\nu = 26\text{--}124$ eV) photons ionize He I, and recombination efficiently populates the 2^3S triplet state, which is metastable and can only decay to the ground state through forbidden transitions. While EUV photons populate the 2^3S state by supplying He ions, mid-ultraviolet (mid-UV) ($h\nu = 4.8\text{--}10$ eV) photons act to depopulate it through photoionization. Thus, tracing mass loss with this method is sensitive to the host star’s SED, specifically the EUV/mid-UV ratio. Planets orbiting K stars fall into this region for optimal He I 10830 Å observability (Oklopčič 2019).

The first successful He I 10830 Å detection was made by Spake et al. (2018), who detected an extended exosphere of the sub-Saturn WASP-107b. Since then, there has been a flurry of mass-loss detections using He I 10830 Å for close-in planets orbiting late-type stars.

Another early detection was of WASP-69b, a $1.1 R_J$, $0.26 M_J$ planet that orbits a K5 type host once every 3.86 days. Nortmann et al. (2018) previously observed He I 10830 Å absorption in the system with the CARMENES spectrograph at Calar Alto Observatory. Over 2 nights, Nortmann et al. reported a relative excess He I absorption of 3.59% with a net blueshift of -3.58 km s⁻¹. They detected no observable pre-transit absorption but reported continued absorption for 22 minutes post-transit, which suggests asymmetry in the outflow geometry resembling a comet-like tail.

In another observation of WASP-69b, Vissapragada et al. (2020) used an ultra-narrowband filter coupled to a beam-shaping diffuser on the Wide-field Infrared Camera (WIRC) at Palomar Observatory. They reported an excess He I absorption of $0.498\% \pm 0.045\%$ during transit, which is consistent with previous observations when considering their bandpass; however, they did not detect any He I trailing the planet. We

Table 1
WASP-69b: Physical, Orbital, and System Parameters

Parameter	Unit	Value	Reference
T_{eff}	[K]	4700 ± 50	Casasayas-Barris et al. (2017)
Age	[Gyr]	7.0	Casasayas-Barris et al. (2017)
Fe/H	...	0.150 ± 0.080	Bonomo et al. (2017)
M_*	$[M_{\odot}]$	0.826 ± 0.029	Casasayas-Barris et al. (2017)
R_*	$[R_{\odot}]$	0.813 ± 0.028	Casasayas-Barris et al. (2017)
$v \sin(i_*)$	$[\text{km s}^{-1}]$	2.20 ± 0.40	Casasayas-Barris et al. (2017)
$\log g$	$[\text{cm s}^{-2}]$	4.50 ± 0.15	Stassun et al. (2017)
γ	$[\text{km s}^{-1}]$	-9.62826 ± 0.00023	Anderson et al. (2014)
M_p	$[M_J]$	0.2600 ± 0.0185	Casasayas-Barris et al. (2017)
R_p	$[R_J]$	1.057 ± 0.017	Casasayas-Barris et al. (2017)
T_{eq}	[K]	963 ± 18	Casasayas-Barris et al. (2017)
K_p	$[\text{m s}^{-1}]$	38.1 ± 2.4	Casasayas-Barris et al. (2017)
a	[au]	0.04525 ± 0.00075	Casasayas-Barris et al. (2017)
a/R_*	...	12.00 ± 0.46	Casasayas-Barris et al. (2017)
T_c	[BKJD]	915.8334 ± 0.0002	Casasayas-Barris et al. (2017)
P	[d]	3.8681390 ± 0.0000017	Casasayas-Barris et al. (2017)
T_{14}	[hr]	2.23 ± 0.023	Casasayas-Barris et al. (2017)
i_p	[deg]	86.71 ± 0.20	Casasayas-Barris et al. (2017)
e	...	0	Casasayas-Barris et al. (2017)
b	...	0.686 ± 0.023	Casasayas-Barris et al. (2017)

note that the photometric observations do not contain velocity information.

In this paper, we provide a new view of the WASP-69b outflow using Keck/NIRSPEC. Relative to CARMENES, NIRSPEC collects more photons per transit, resulting in a higher signal-to-noise (S/N) and allows for a more detailed examination of the tail geometry and velocity structure.

We describe our Keck/NIRSPEC observations in Section 2. We explain the data reduction process in Section 3. We characterize the strength, time dependence, and velocity structure of the outflow in Section 4. We estimate the mass-loss rate in Section 5. We discuss comparisons with previous observations and place our observations of WASP-69b in the broader context of He I detections in Section 6. Finally, we conclude in Section 7 with a discussion of our WASP-69b interpretation and potential future work on this system as well as others.

2. Observations

On 2019 July 12 UT, we observed the transit of WASP-69b (see Table 1 for system parameters) using Keck/NIRSPEC (McLean et al. 1998; Martin et al. 2018). We used the NIRSPEC-1 filter ($\lambda = 9470\text{--}11210 \text{ \AA}$) and the $0''.28 \times 12''$ slit, which provides a resolving power of $R = 40,000$; at the He feature, this corresponds to $\Delta\lambda = 0.3 \text{ \AA}$ or $\Delta v = 7.5 \text{ km s}^{-1}$. Following previous works, we removed the “thin” blocking filter to eliminate CCD fringing in the Y-band. On 2022 August 2 UT we observed WASP-69 again using the same setup and reduction listed throughout this paper. However, due to a time-scheduling error, we did not observe the transit of WASP-69b. However, this did allow us to obtain an out-of-transit baseline for WASP-69, which we use to further constrain He I variability in the stellar atmosphere. These observations occurred during orbital phase $\phi = [-0.30, -0.22]$ compared to the transit midpoint at phase of $\phi = 0$.

We scheduled our observations using the ephemeris of Casasayas-Barris et al. (2017). The transit midpoint occurred at

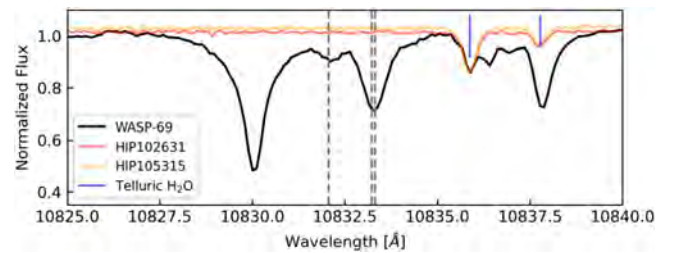


Figure 1. The two calibration stars, HIP102631 (red) and HIP105315 (orange), are shown here with a slight offset. The nearby telluric absorption features at 10835.9 and 10837.8 \AA are marked with blue. A representative WASP-69 exposure is shown in black and conveys the spectral region, instrument resolution, and signal-to-noise ratio. The three dashed gray lines indicate the He I 10830 \AA triplet vacuum rest wavelengths. The main core of the profile comes from the 10833.22 and 10833.31 \AA features, which are blended. The weaker singlet is located at 10832.06 \AA .

$12:20 \text{ UT}$ with ± 2.1 minute midpoint uncertainty. We used the ABBA nod-dithering technique to remove signal from the background and collected 104 exposures of WASP-69 with integration times of 149 s from UT = 09:25–14:44. The first observation began 108 minutes before ingress when the target was at airmass = 1.44; the last observation ended when the target was at airmass = 1.46. We lost guiding on two frames in the WASP-69 sequence during egress. Additionally, we observed two nearby rapidly rotating A0V stars for telluric calibration at the beginning and end of the WASP-69 observing sequence: HIP102631 (airmass = 1.35, $v \sin(i) = 142 \text{ km s}^{-1}$) and HIP105315 (B9V, airmass = 1.62, $v \sin(i) = 200 \text{ km s}^{-1}$).

3. Data Reduction

We reduced 104 raw observations using the NIRSPEC Reduction Package, REDSPEC (Kim et al. 2015).⁴ We focused

⁴ <https://github.com/Keck-DataReductionPipelines/NIRSPEC-Data-Reduction-Pipeline>

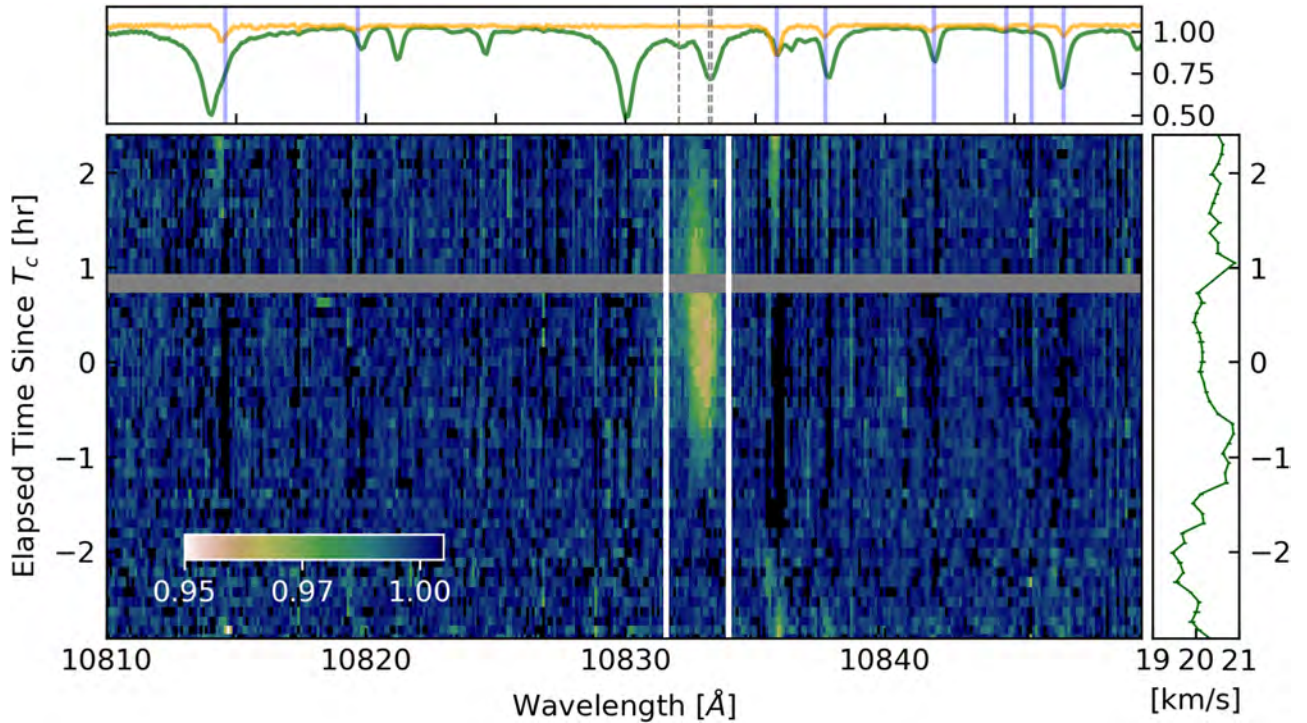


Figure 2. Colors in the main panel show the depth of each normalized spectrum *relative* to a master template made up of all pre-transit observations, i.e., 1.0 corresponds to no excess absorption. Missing data are gray, and the vertical white lines encompass the defined He I bandwidth (see Section 2 for further details). The top panel shows the green master spectrum for WASP-69 and the orange HIP105315 telluric standard spectrum for which we have applied an arbitrary vertical offset for clarity. Telluric absorption features are indicated with blue vertical lines and coincide with the transient vertical artifacts in the plot. The right panel shows the velocity shift between the PHOENIX model and each frame.

Table 2
Observations

Target	Observation	Date of observation	Start Time (UT)	End Time (UT)	Airmass range	N_{obs}	t_{exp} (s)	S/N per pixel range
HIP102631	Telluric Std	2019-07-12	09:09	09:12	1.36–1.34	4	50	50
WASP-69	Pre-Transit	2019-07-12	09:25	11:06	1.44–1.14	34	149	35–60
WASP-69	In-Transit	2019-07-12	11:09	13:32	1.13–1.19	42	149	50–62
WASP-69	Post-Transit	2019-07-12	13:36	14:47	1.20–1.48	24	149	51–58
HIP105315	Telluric Std	2019-07-12	14:59	15:06	1.6–1.64	4	100	50
WASP-69	Out-of-Transit	2022-08-02	05:58	13:45	1.07–3.47	74	149	25–42

on échelle order 70, which encompasses the He I triplet transition lines. In this work, we adopt a vacuum wavelength scale for the He I triplet transitions (10832.06, 10833.22, and 10833.31 Å). We established our laboratory wavelength solution using Neon, Argon, Xenon, and Krypton arc lamps provided by NIRSPEC website.⁵

We derived an initial wavelength solution and reduced each AB and BA nod pair into single, combined 1D frames. We used the suggested S/N measurement formula for the 2018 NIRSPEC update and report a S/N of ≈ 55 per reduced pixel. Due to the target hopping off of the slit mentioned in the previous section, there is a small gap of missing data in our time series that occurs just as the planet begins egress.

We used REDSPEC to identify bad pixels and cosmic-ray hits and interpolated over them using a cubic spline.

We used the calibration star spectra to identify telluric features in the target spectrum and inspect for contamination of the He I profile. We identify nearby H₂O absorption lines at

10835.9 and 10837.8 Å, but they do not interfere with the absorbing He I band as shown in Figure 1.

We shifted the spectra to the stellar rest frame by cross-correlating each spectrum with a PHOENIX stellar template model (Husser et al. 2013) with the following parameters: $T_{\text{eff}} = 4700$ K; $\log(g) = 4.5$; $[M/H] = 0.0$. We masked out the He I absorbing region (10830–10835 Å) as well as any telluric features so they do not influence our spectral registration.

We fit the resulting cross-correlation function peaks with Gaussian profiles and determined velocity shifts for each spectrum. These shifts ranged from 19 to 21 km s⁻¹ and included barycentric Doppler shifts and instrument variability. With our observations now shifted into the stellar rest frame, we co-added the spectra into three distinct bins: pre-transit, in-transit, and post-transit (see Table 2). We computed the average spectrum for each bin and plot the composite spectra and corresponding shifts in Figure 2. To interpret the outflow with respect to the WASP-69b, we now calculate the projected velocity of the planet and shift the spectra into the planetary rest frame.

⁵ <https://www2.keck.hawaii.edu/inst/nirspec/lines.html>

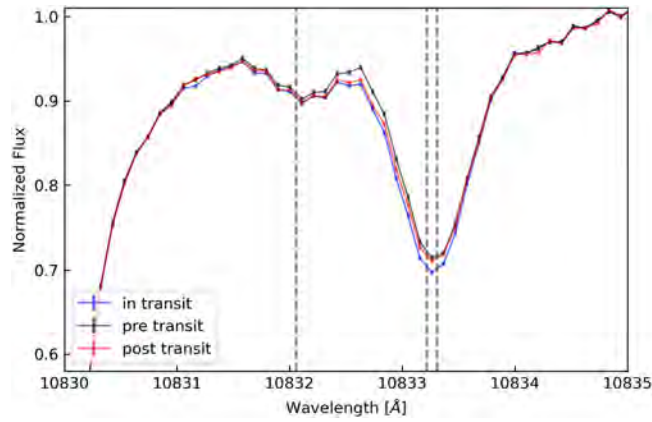


Figure 3. The He I feature is deeper in-transit (blue spectrum) and post-transit (red spectrum) compared to pre-transit (black spectrum). Gray dashed lines represent the central rest wavelengths in the stellar rest frame.

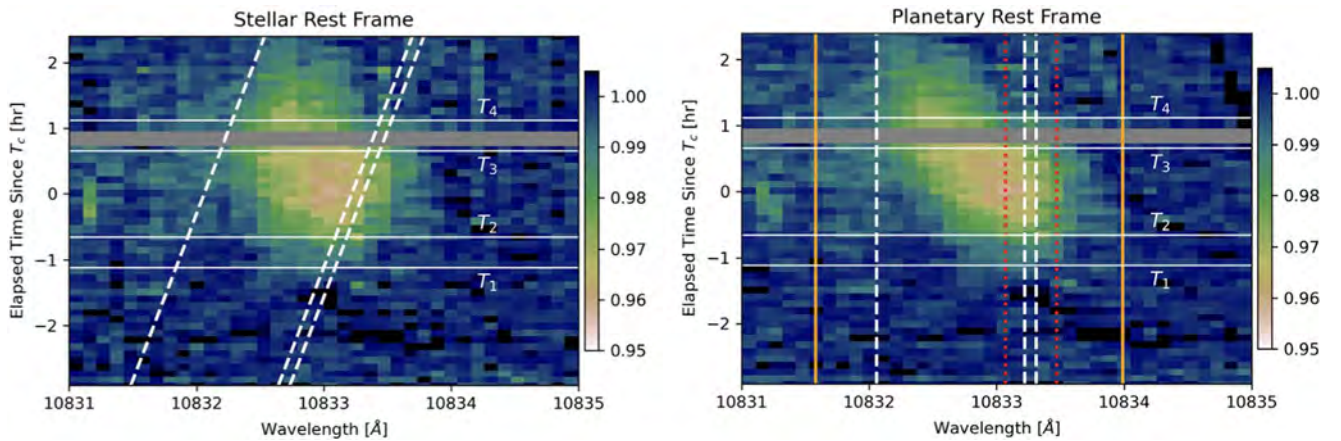


Figure 4. Left: same as Figure 2 but detailing the He I triplet. T_1 , T_2 , T_3 , and T_4 label the four transit contact times. The three white dashed lines represent the expected motion of the He I transition lines in the stellar rest frame due to the predicted planetary velocity. Right: same as left but shifted into the planetary rest frame. Two separate helium bandpasses used to sum up the helium light curve are plotted as vertical orange solid line and red dotted lines. The orange vertical lines represent our preferred bandpass. The red dotted lines are comparable to the bandpass used in other data sets.

4. Results

In Figure 3, we show the normalized pre-transit, in-transit, and post-transit absorption profiles in the He I band with respect to the central rest wavelength positions of the He I triplet. Excess absorption is clearly visible in-transit and post-transit. The difference in absorption depth and width of the bluer wing of the profile is evident.

In Figure 4, we plot the relative absorption intensity in both the stellar and planetary rest frames. The first through fourth contact points are shown as well as the central positions of the He I 10830 Å triplet. We report an average in-transit absorption depth of $2.7\% \pm 0.4\%$. We estimated the uncertainty over the He I 10830 Å bandwidth [10831.58–10833.99 Å] by measuring the standard deviation of the average normalized intensity in neighboring bins of equal extent in time and wavelength. This dispersion captures the photon-counting statistics and instrumental errors associated with variations in wavelength solution and line profile. Assuming a spherical outflow geometry, the relative absorption depth tells us about the extent to which the extended exosphere is enveloping the planet.

We computed the velocity of the He I triplet by modeling the profile of the line with 3 Gaussians, each corresponding to the

three central wavelengths of the metastable He I transition. We fixed the relative heights and wavelength between the transitions and allowed two parameters to vary: the total depth and the central wavelength. During the in-transit observations, we detect a net blueshift of $-5.9 \pm 1.0 \text{ km s}^{-1}$. This radial velocity shift in the absorption profile can trace the bulk velocity structure of the outflowing He I.

We can see that the excess absorption continues for the entire post-transit sequence (1.28 hr). Furthermore, the absorbing He I is blueshifted for the duration of the transit and accelerates away from the star. This excess He I absorption post-transit is consistent with a “comet-like” tail of helium trailing the planet and continuing to absorb stellar photons while being accelerated away from the planet and toward the observer due to stellar winds. As the planet has traveled over $7 R_p$ beyond the disk, a continually thinning column of He I is still detected.

These tails are shaped by stellar winds that interact with the planetary outflow and redirect material around the planet, radially away from the star (MacLeod & Oklopčić 2022). McCann et al. (2019) showed that the degree to which the planetary outflow is shaped is a function of orbital velocity,

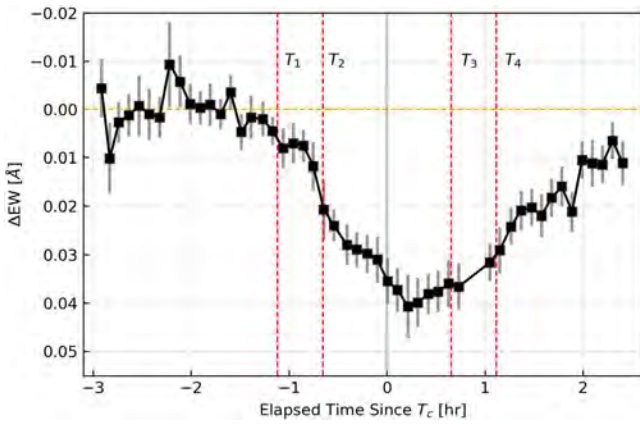


Figure 5. Equivalent width variations over the course of the night. The red dashed lines represent the four contact points, and the horizontal orange dashed line shows the pre-transit baseline, which is not recovered. The maximal depth is slightly delayed compared to mid-transit, as predicted by modeling strong stellar wind interactions that shape planetary outflows.

intrinsic planetary wind velocity, and stellar wind strength—which can be variable itself. While weak stellar winds cannot confine the planetary outflow, a strong stellar wind can suppress the outflow and redirect the majority of the out-gassed material into the tail. Observational evidence of this was first seen in Ly α detections, the most extreme for the hot-Neptune GJ436b (Lavie et al. 2017) which has a hydrogen tail that continues absorbing for several hours after the optical transit ends.

The time asymmetry of the absorption profile is consistent with interactions between planetary outflows and strong stellar winds (MacLeod & Oklopčić 2022). In general, a planetary outflow will form a bow shock at the point where the outflow ram pressure ρv^2 equals the ram pressure of the stellar wind. Multiple groups have shown that for sufficiently strong stellar winds, the planetary outflow can be suppressed

below the sonic surface and completely redirected around the planet and toward the tail (Wang & Dai 2021a; MacLeod & Oklopčić 2022).

To probe the extent of the absorption, we computed the equivalent width for the spectral time series. We defined the He I absorbing band [10831.58–10833.99 Å] to include the full wavelength range where excess absorption is detected (Figure 2).

We report a maximum EW just after mid-transit of $40.7 \text{ m}\text{\AA} \pm 6.8 \text{ m}\text{\AA}$. During the transit (T_{14}), we find an average equivalent width (EW) of $27.8 \text{ m}\text{\AA} \pm 2.5 \text{ m}\text{\AA}$. As shown in Figure 5, the post-transit equivalent width never returns to the pre-transit baseline. We compute an average EW of $15.4 \text{ m}\text{\AA} \pm 3.9 \text{ m}\text{\AA}$ during the post-transit phase. Here the time asymmetry can be seen clearly, and in the last observation (1.28 hr after T_4) we report an EW 5% higher than the pre-transit average.

Simulations show that stellar winds can not only cause time asymmetry in the relative equivalent width absorption of the He I feature but also shift the peak of maximal absorption relative to the optical point of conjunction (Wang & Dai 2021a; MacLeod & Oklopčić 2022). After the peak absorption, the decrease in absorption transitions in to a more gradual return to the pre-transit baseline that can take several hours.

Assuming a circular orbit, we calculate WASP-69b’s orbital velocity $v_{\text{orb}} = 2\pi a_p/P = 127.3 \pm 1.5 \text{ km s}^{-1}$. In the 1.28 hr of post-transit observations that we detect continued absorption, the planet travels $\sim 5.9 \times 10^5 \text{ km}$. Assuming all of the helium we are seeing is confined to a partial annulus at the orbital separation of the planet, we set a minimum limit on the length of the He I tail $\geq 7.5 R_p$. The Roche lobe for WASP-69b is located at $\approx 2.7 R_p$, but the tail extends well beyond that limit and is unbound from the gravitational influence of the planet. A simple diagram of the transit chord can be seen in Figure 6.

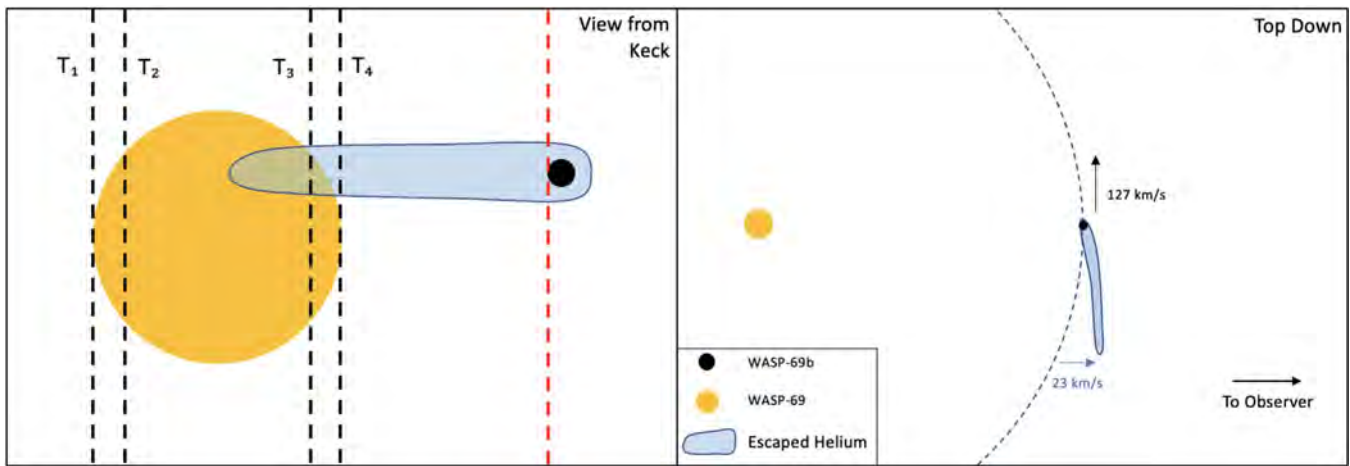


Figure 6. Transit chord and top-down view of the WASP-69 system presented to scale. Left: transit chord view from Keck. The four contact points, T_1 , T_2 , T_3 , and T_4 are represented with vertical black dashed lines and the absorbing He I is light blue. The red dashed line represents the final predicted position of the planet corresponding to the last observation in the spectral time series after traveling over $7 R_p$ (1.28 hr) beyond the disk of the star from the perspective of the observer. Right: top-down view of the system. The He I tail can be seen accelerating toward the observer on the lower right of the panel.

5. Mass-loss Rate Estimate

One of the main goals for tracing He I is to quantitatively measure mass-loss rates in real time. A detailed model of this outflow would include effects like Coriolis force and advection coupled with a 3D radiative transfer scheme and is beyond the scope of this work (see, e.g., Wang & Dai 2021b). Here, we offer two estimates of the mass-loss rate of WASP-69b: (1) an order-of-magnitude estimate following the method of Zhang et al. (2022) and (2) an estimate assuming a 1D Parker-like outflow.

5.1. Order of Magnitude

We assumed that most of the planetary outflow is optically thin, which is consistent with the weakness of the singlet centered near 10832 Å. We then take the optical depth from star to observer to be

$$\tau(\lambda) = n_{\text{He}} \sigma_{\lambda} P(\lambda), \quad (1)$$

where n_{He} is the column density of metastable helium atoms, $P(\lambda)$ is the line profile with $\int_{-\infty}^{+\infty} P(\lambda) d\lambda = 1$, and the absorption cross section is $\sigma_{\lambda} \equiv (\pi e^2 g_l f_l \lambda_0^2) / (m_e c^2)$. Here, e is the electron charge, m_e is the electron mass, g_l is the statistical weight for the lower level, f_l is the oscillator strengths of the three lines (0.059, 0.179, and 0.299, respectively; Kramida et al. 2022), and λ_0 is the rest wavelength of the absorbing spectral line. Assuming the optically thin limit where $1 - e^{-\tau} \approx \tau$, we integrate over λ and obtain the standard equation for equivalent width:

$$W_{\lambda} = N \sigma_{\lambda}. \quad (2)$$

Defining the average equivalent width W_{avg} , we can solve for the total number of metastable helium atoms $N_{\text{He}^3\text{S}}$ by integrating over and dividing by the cross-sectional area of the star:

$$\begin{aligned} W_{\text{avg}} &= \frac{1}{\iint dS} \iint W_{\lambda} dS \\ \iint W_{\lambda} dS &= W_{\text{avg}} \iint dS \\ N_{\text{He}^3\text{S}} \sigma_{\lambda} &= W_{\text{avg}} \pi R_{*}^2 \\ N_{\text{He}^3\text{S}} &= \frac{R_{*}^2 m_e c^2}{e^2 g_l f_l \lambda_0^2} W_{\text{avg}}. \end{aligned} \quad (3)$$

Using our calculated EW measurement for W_{avg} , we calculate $N_{\text{He}^3\text{S}} = 3.1 \times 10^{32}$, which we can convert into a total amount of helium, assuming metastable helium comprises 10^{-6} of total helium nuclei. This fraction assumes an optimistic case that applies to early K-type stars (as shown in Oklopčić 2019). Assuming primordial mass and number composition ratios for helium to hydrogen, 3:1 and 9:1 respectively, we estimate the total mass of the planetary outflow in helium and hydrogen to be $m_{\text{tot}} = 1 \times 10^{16}$ g. With this mass estimate, we can estimate a total mass-loss rate m_{tot}/τ , where the replenishment lifetime for observable He I atoms crossing the stellar disk is $\tau = R_{*}/c_s$ and where c_s is the sound speed. We adopt 10 km s^{-1} , which is consistent with a typical sound speed for planets with these outflows. Our order-of-magnitude mass-loss estimate is $\dot{M} = m_{\text{tot}}/\tau = 1 M_{\oplus} \text{ Gyr}^{-1}$ or $1.8 \times 10^{11} \text{ g s}^{-1}$.

5.2. One-dimensional Parker Model

As an alternative to our order-of-magnitude estimate, we use p-winds (Dos Santos et al. 2022) to estimate a mass-loss rate by fitting a Parker wind model to our observations. p-winds is an open-source code that implements the 1D model described by Oklopčić & Hirata (2018) and Lampón et al. (2020) and takes as input the stellar XUV spectrum and the observed Helium transmission spectrum.

As noted, the 1D model is insufficient for modeling outflows with significant asymmetry; however, it is a useful point of comparison to our order-of-magnitude model and to previous observations. Since the X-ray and ultraviolet (XUV) spectrum of WASP-69 is not known, we obtained the MUSCLES XUV spectrum ($\lambda = 10\text{--}1000 \text{ \AA}$ $h\nu = 1200\text{--}12 \text{ eV}$) of similar star HD85512 (K5) as a proxy for WASP-69. The MUSCLES spectra are observed XUV fluxes at Earth, which are then scaled to the appropriate semimajor axis for WASP-69b.

With p-winds, we derived a sound speed of 9 km s^{-1} at the sonic point, which occurs at $\sim 3 R_p$. For a Parker-type hydrodynamic wind, this effectively represents the regime where the pressure-driven flow is no longer being controlled by the planet's gravity. We derived a temperature in this part of the thermosphere of $9900 \pm 900 \text{ K}$. We found the total fraction of helium in the metastable state to be 5.4×10^{-6} , in agreement with the optimistic case for the environment around a K-type star (Oklopčić 2019). The estimated mass-loss rate for the 1D model is $m_{\text{tot}}/\tau = 1 M_{\oplus} \text{ Gyr}^{-1}$ ($2.0 \times 10^{11} \text{ g s}^{-1}$).

We note as a sanity check that the assumptions made in our order-of-magnitude estimate are comparable with the p-winds 1D results. Given the difference in these approaches, the agreement is better than expected, and we trust both methods at the order-of-magnitude level.

Assuming a constant orbital distance and stellar output over time, the current mass-loss rate suggests that WASP-69b has lost $\sim 7 M_{\oplus}$ over the course of the system's $\sim 7 \text{ Gyr}$ lifetime. At the current rate, WASP-69b ($92 M_{\oplus}$) is not at risk of losing its envelope before the end of the lifetime of the system.

In the 2022 out-of-transit spectrum for WASP-69, which can be seen in Figure 7, we measured a variability over the main core of the stellar He I triplet of 0.29% throughout the night. These variations fall below our noise floor. We report a pre-transit EW average in 2019 of $0.23 \pm 0.03 \text{ \AA}$. We compare this to the averaged EW we measured for the 2022 WASP-69 out-of-transit time series of $0.18 \pm 0.03 \text{ \AA}$. The absolute difference in EW between both out-of-transit epochs is $0.05 \pm 0.06 \text{ \AA}$. While we do not see any evidence for significant variation within the night on 2022, this does not rule out more long-term variability in the stellar He I line, or that the pre-transit EW from 2019 was partially contaminated by the “leading arm” of the planetary outflow.

6. Comparison to Previous Observations

Our in-transit analysis is consistent with previous CARMENES observations made by Nortmann et al. (2018), who reported a blueshift of $-3.58 \pm 0.23 \text{ km s}^{-1}$ and $3.59\% \pm 0.19\%$ excess absorption (compared to our values $-5.9 \pm 1.0 \text{ km s}^{-1}$ and $2.7\% \pm 0.4\%$ excess absorption). We note here that our values are measured from an average of the entire transit (T_{14}), whereas the CARMENES values come from the average during T_{23} when the signal is the strongest. Although our measured values are in agreement, this difference

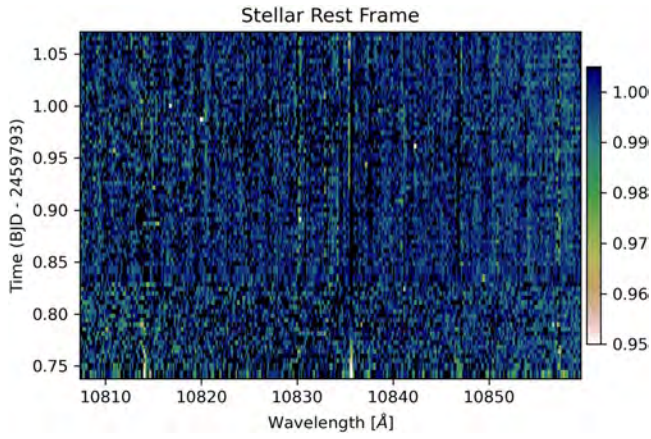


Figure 7. WASP-69 out-of-transit spectral time series for 2022 August 2. We measure a variability over the He I triplet band of 0.29% and report an average equivalent width of $0.18 \pm 0.03 \text{ \AA}$

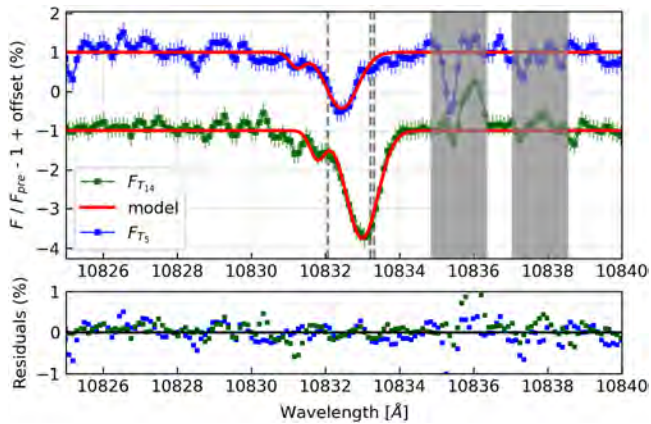


Figure 8. The green points show the averaged in-transit transmission spectrum of He I 10830 Å absorption. The blue points show the averaged post-transit transmission spectrum, which is significantly blueshifted ($-23.3 \pm 1.0 \text{ km s}^{-1}$). The gray vertical masks cover nearby telluric features, and the residuals of the models are shown in the bottom panel.

does result in a lower reported absorption during our analysis. However, our post-transit results are inconsistent with their measurements. Nortmann et al. (2018) reported an average post-transit absorption of 0.5% and net blueshift of $-10.7 \pm 1.0 \text{ km s}^{-1}$. During the same phase, we detected an average post-transit absorption of $1.5 \pm 0.2\%$ and a net blueshift of $-23.3 \pm 0.9 \text{ km s}^{-1}$ (Figure 8). This is a significant difference and can be seen in the helium light-curve comparison for the post-transit sequence in Figure 9. The scatter in the CARMENES data is much higher than the formal uncertainties. Note that this visualization is highly dependent on the choice of bandpass for helium absorption. CARMENES ($R = 80,000$) has a higher resolution than NIRSPEC ($R = 40,000$), but it is on a 3.5 m telescope and collected 8 times fewer photons per transit. The 10 m Keck II dish allowed us to get significantly higher S/N per pixel (~ 55 compared to ~ 18 for the CARMENES observations), which likely explains the reported differences between our measurements. In Figure 10 we plot our 2019 He I transmission spectrum with the 2 nights of data provided by Nortmann et al. (2018) during T_{23} . The He I 10830 Å triplet is well resolved in both sets of observations. When the signal is the strongest, there is less discrepancy between the data sets. However, when the He I becomes more diffuse, the S/N differences between

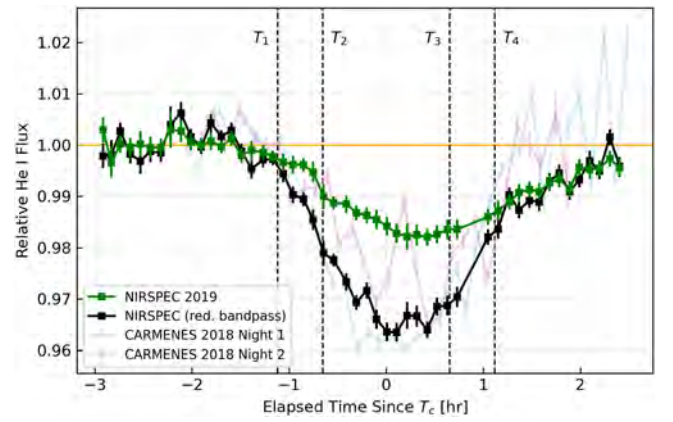


Figure 9. Helium light curves plotted from this work and 2 nights of CARMENES observations from Nortmann et al. (2018). The NIRSPEC observations never return to the baseline post-egress (green). The CARMENES observations do return to the baseline helium absorption level, at least within the achieved precision. Note that for the CARMENES data the point-to-point scatter is significantly higher than the formal uncertainties, which suggests systematic errors or are simply the effects of a reduced signal with lower S/N. Plotted in black is the NIRSPEC data but with a reduced bandpass that is consistent with the He I bandpass of Nortmann et al. (2018) [10833.07–10833.47 Å] for a better comparison. Our preferred bandpass (green points) [10831.58–10833.99 Å] allows us to detect lower levels of He I absorption in the post-transit sequence due to the high S/N of NIRSPEC. Both helium bandpasses can be seen plotted in Figure 4.

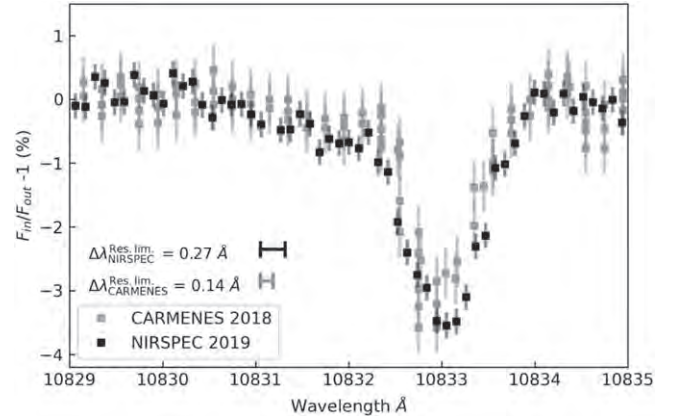


Figure 10. He I 10830 Å absorption during $T_2 - T_3$ from Nortmann et al. (2018) and this work. For reference, the resolving limits are plotted for both instruments. The He I 10830 Å line is clearly resolved in both cases. Thus, we can rule out instrument resolution-dependent variability between these data sets.

the two instruments is the likely cause for the observed variability in the post-transit tail length. Vissapragada et al. (2020) reported comparable S/N per pixel as the CARMENES data set, so the lack of significant post-transit He I absorption in the WIRC observations can also be explained by lower S/N levels.

The previous CARMENES observations from Nortmann et al. (2018) were used in a 3D Hydrodynamics model by Wang & Dai (2021b). They reported a mass-loss rate $\sim 0.5 M_{\oplus} \text{ Gyr}^{-1}$ for WASP-69b but no helium tail. Those results seem consistent with the data set they used. Similarly, Vissapragada et al. (2020) report a mass-loss rate of $\sim 0.2 M_{\oplus} \text{ Gyr}^{-1}$, which they computed using the same p-winds 1D model that assumes a symmetrical planetary outflow (Oklopčić & Hirata 2018). Our mass-loss rate estimate

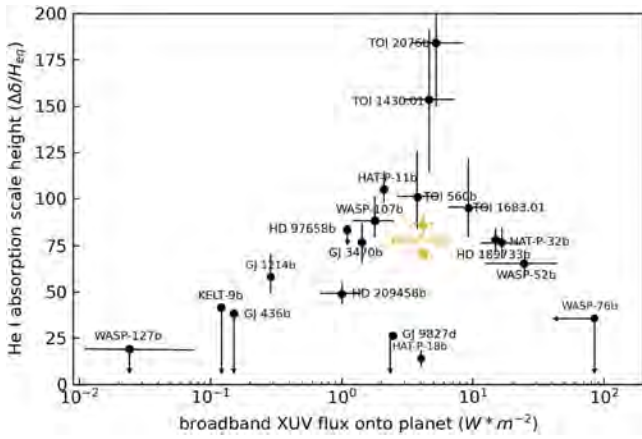


Figure 11. Summary of He I 10830 Å detections. Equivalent height δ_{R_p} is normalized by the atmospheric scale height H_{eq} and plotted vs. broadband XUV flux the planet receives. The WASP-69b observations are both colored orange, with the results from this work marked with a star. Note that the two WASP-69b data points agree when the transit depth is averaged over the same phase of the transit. Data for other known He I 10830 Å detections taken from multiple references (i.e., Kohler 2018; Nortmann et al. 2018; Salz et al. 2018; Alonso-Floriano et al. 2019; Gaidos et al. 2020; Ninan et al. 2020; Kasper et al. 2020; Vissapragada et al. 2020; dos Santos et al. 2020; Casasayas-Barris et al. 2021; Paragas et al. 2021; Spake et al. 2021; Vissapragada et al. 2021; Kirk et al. 2022; Orell-Miquel et al. 2022; Czesla et al. 2022; Zhang et al. 2022; Zhang et al. 2023).

of $1.0 M_{\oplus} \text{Gyr}^{-1}$ is higher than both previous results but within an order of magnitude. We require hydrodynamic 3D-modeling for the most accurate mass-loss estimate for WASP-69b.

Spake et al. (2021) observed the WASP-107 system with NIRSPEC and reported similar results to these. WASP-107b ($M_p = 0.1 M_J$, $R_p = 0.9 R_J$) has a 5.7 day orbital period around a $0.7 M_{\odot}$ host star. They reported continued He I absorption for over an hour post-transit, which corresponds to a He I tail length of 5.0×10^5 km. At the time, this was the most dramatic post-transit He I tail observed. At the lower limit of 5.8×10^5 km, the tail of WASP-69b is at least that long.

Another common indicator for the extent of He I abundance is the equivalent height of the absorbing atmosphere (Nortmann et al. 2018). Equivalent height is a useful parameter to characterize the radius of the planet in the He I 10830 Å profile. Equivalent-height is defined as $\delta_{R_p} = (\Delta d R_*^2 + R_p^2)^{1/2} - R_p$, where Δd is the transit depth in He I. We can compare this equivalent height to the lower atmospheric scale height $H_{\text{eq}} = (k_B T_{\text{eq}}) / (\mu g)$, where $\mu = 2.3 \times m_{\text{H}}$, which is consistent with a solar H–He composition, to determine how extended the absorbing atmosphere is beyond the expected opaque limit of the atmosphere of a planet with a given temperature.

Figure 11 shows all of the He I 10830 Å detections that we are aware of in the literature⁶ and shows the 2 WASP-69b detections plotted in orange (this work indicated with a star). For WASP-69b, using our average absorption over the full transit ($T_1 - T_4$) of $2.7\% \pm 0.4\%$, we compute $\delta_{R_p} / H_{\text{eq}} = 66.1 \pm 3.1$. We note that our $/H_{\text{eq}}$ estimate is about $\sim 25\%$ less than the value 85.5 ± 3.6 reported by Nortmann et al. (2018), but this is only due to a choice of when to average over

the transit chord. Nortmann et al. (2018) report the average during T_{23} , when the absorption is deeper. Similarly, during T_{23} of our time series, we measure an average absorption depth of $3.6\% \pm 0.5\%$ and $\delta_{R_p} / H_{\text{eq}} = 83.1 \pm 3.9$. While we opt to report the standard average absorption over the course of the transit, we note that these equivalent-height values are in agreement.

Here we highlight a practical limit for the equivalent-height metric as a mode of comparison between He I absorption detections. Because of the dependence on transit depth Δd , instruments with different resolutions may not derive the same equivalent height for the same object. As spectral resolution, $R = \frac{\lambda}{\Delta\lambda}$, increases, spectral features appear narrower and deeper. For lower resolution, the same feature will become broadened and shallow. Thus, the transit depth for the same system can vary across instruments (or with slit width within the same instrument). However, what will remain constant is the total area under the absorption curve.

We suggest a metric that translates better across observation and instrument parameters such as “equivalent width time” $\int EW dt$ over the full transit/tail duration. In the case of partial transits, an alternative measurement that would make sense is equivalent width per unit orbital phase. This yields a single number that would normalize comparisons across observations/instruments in a convenient way. For our observations, we compute $\int EW dt = 297 \pm 50 \text{ Å s}$. We did not reanalyze other existing data sets to compute this quantity, but such an effort would bring additional clarity into the census of helium outflows.

Although we can confidently attribute a significant portion of the observed variability of this system to differences in S/N between instruments, stellar variability may also contribute. There are at least three known sources of stellar variability that could be causing epoch-dependent variations in the He I transit depth/morphology/velocity structure.

The first is that the He I 10830 Å feature varies in the stellar atmosphere. However, this seems unlikely, and we did not measure significant relative He I absorption variability in any of our out-of-transit observations for WASP-69.

The second source of stellar variability could come from relative changes in output from different parts of the star’s electromagnetic spectrum. Although the 2^3S metastable state is most efficiently populated by the EUV/FUV flux ratio of K-type stars like WASP-69, the extent of variability of those outputs is not well constrained. Perhaps the tail is significant, but the fluctuating stellar EUV/FUV levels act as a sort of variable light source behind the outflow, adjusting the contrast of what regions of it the observer can detect. As the EUV/FUV flux ratio becomes more favorable for the metastable state, we can see lower regions of column density, while higher density regions become optically thick, and vice versa.

A third source of stellar variability could come from variations in the stellar wind strength. Work by MacLeod & Oklopčić (2022) on modeling the extended tail for WASP-107b demonstrates many of the features we find in our observations: a delayed absorption peak relative to optical transit, an asymmetrical He I light curve, and an accelerating blueshift of gradually decreasing He I absorption hours after egress. These traits are consistent with interactions of a planetary outflow being suppressed and redirected due to a strong stellar wind. This would indicate variability in the physical length of the tail and could explain why we measured a $\geq 7.5 R_p$ length tail compared to $2.2 R_p$ from Nortmann et al. (2018) in observations made 1 yr prior.

⁶ Kohler (2018); Nortmann et al. (2018); Salz et al. (2018); Alonso-Floriano et al. (2019); Gaidos et al. (2020); Ninan et al. (2020); Kasper et al. (2020); Vissapragada et al. (2020); dos Santos et al. (2020); Casasayas-Barris et al. (2021); Paragas et al. (2021); Spake et al. (2021); Vissapragada et al. (2021); Kirk et al. (2022); Orell-Miquel et al. (2022); Czesla et al. (2022); Zhang et al. (2022); Zhang et al. (2023).

It is possible that all three of the sources of stellar variability mentioned above are linked to one another; they should all vary with overall variations in stellar activity.

7. Conclusion

In this work, we present high-resolution transmission spectroscopy of the metastable He I 10830 Å absorption feature for the WASP-69b transit on 2019 July 12 UT. During the transit (T_{14}) we detect an average relative helium absorption level of $2.7\% \pm 0.4\%$ and a net blueshift of $-5.9 \pm 1.0 \text{ km s}^{-1}$. These values are consistent with the in-transit observations from Nortmann et al. (2018). The absorption signal is also consistent with Vissapragada et al. (2020).

However, we detect continued post-transit absorption of He I, which is not seen in the other observations. This extended absorption lasts for at least 1.28 hr post-transit and never returns to the pre-transit baseline. We set a lower limit for the helium tail $\geq 7.5 R_p$.

We attribute most of this variability to the high S/N per pixel NIRSPEC achieves, allowing the detection of smaller amounts of He I and over a longer period of time. While instrumental differences surely play a role in these discrepancies, variations within the star or complicated planetary atmosphere dynamics could also be responsible.

The asymmetry in the helium absorption curve is consistent with an outflow being shaped by a strong stellar wind and requires 3D hydrodynamic modeling for the most accurate mass-loss estimate. However, we estimate a mass-loss rate of $1 M_{\oplus} \text{ Gyr}^{-1}$, which we trust within an order of magnitude.

Repeat observations are valuable to probe any variability in the outflow properties, especially with different instruments. There is likely variability stemming from multiple sources. Neither stellar wind strength or EUV/mid-UV output variability is well understood for stars other than our Sun, so planetary outflow observations such as these may be a useful method for studying and constraining certain types of stellar variability.

Acknowledgments

The helium data presented herein were obtained at the W. M. Keck Observatory, which is operated as a scientific partnership among the California Institute of Technology, the University of California and the National Aeronautics and Space Administration. The Observatory was made possible by the generous financial support of the W. M. Keck Foundation. We thank the referee for a thorough review that helped improve the quality of this work.

We thank Lisa Nortmann for providing us with the CARMENES data for WASP-69b which was helpful in comparing results between observations. We also thank Michael Zhang and Fei Dai for useful conversations regarding planetary helium outflows. We would also like to thank Greg Gilbert for helpful edits of this manuscript. D.T. is supported in part by the Cota-Robles Fellowship at UCLA, which was instrumental in the advancement of this research.

ORCID iDs

Dakotah Tyler  <https://orcid.org/0000-0003-0298-4667>
 Erik A. Petigura  <https://orcid.org/0000-0003-0967-2893>
 Antonija Oklopčić  <https://orcid.org/0000-0002-9584-6476>
 Trevor J. David  <https://orcid.org/0000-0001-6534-6246>

References

- Alonso-Floriano, F. J., Snellen, I. A. G., Czesla, S., et al. 2019, *A&A*, **629**, A110
- Anderson, D. R., Collier Cameron, A., Delrez, L., et al. 2014, *MNRAS*, **445**, 1114
- Bonomo, A. S., Desidera, S., Benatti, S., et al. 2017, *A&A*, **602**, A107
- Casasayas-Barris, N., Orell-Miquel, J., Stangret, M., et al. October 2021, *A&A*, **654**, A163
- Casasayas-Barris, N., Palle, E., Nowak, G., et al. 2017, *A&A*, **608**, A135
- Czesla, S., Lampón, M., Sanz-Forcada, J., et al. 2022, *A&A*, **657**, A6
- dos Santos, L. A., Ehrenreich, D., Bourrier, V., et al. 2020, *A&A*, **640**, A29
- Dos Santos, L. A., Vidotto, A. A., Vissapragada, S., et al. 2022, *A&A*, **659**, A62
- Fulton, B. J., Petigura, E. A., Howard, A. W., et al. 2017, *AJ*, **154**, 109
- Gaidos, E., Hirano, T., Mann, A. W., et al. 2020, *MNRAS*, **495**, 650
- Husser, T. O., Wende-von Berg, S., Dreizler, S., et al. 2013, *A&A*, **553**, A6
- Kasper, D., Bean, J. L., Oklopčić, A., et al. 2020, *AJ*, **160**, 258
- Kim, S., Prato, L., & McLean, I., 2015 REDSPEC: NIRSPEC data reduction, Astrophysics Source Code Library, ascl:1507.017
- Kirk, J., Dos Santos, L. A., López-Morales, M., et al. 2022, *AJ*, **164**, 24
- Kohler, S. 2018, nova pres, **4320**
- Kramida, A., Ralchenko, Yu., Reader, J. & NIST ASD Team 2022, NIST ASD Team 2022, NIST Atomic Spectra Database (ver. 5.10) (Gaithersburg, MD: National Institute of Standards and Technology), <https://physics.nist.gov/asd>
- Lampón, M., López-Puertas, M., Lara, L. M., et al. 2020, *A&A*, **636**, A13
- Lavie, B., Ehrenreich, D., Bourrier, V., et al. 2017, *A&A*, **605**, L7
- MacLeod, M., & Oklopčić, A. 2022, *ApJ*, **926**, 226
- Martin, E. C., Fitzgerald, M. P., McLean, I. S., et al. 2018, *Proc. SPIE*, **10702**, 107020A
- McCann, J., Murray-Clay, R. A., Kratter, K., & Krumholz, M. R. 2019, *ApJ*, **873**, 89
- McLean, I. S., Becklin, E. E., Bendiksen, O., et al. 1998, *Proc. SPIE*, **3354**, 566
- Ninan, J. P., Stefánsson, G., Mahadevan, S., et al. 2020, *ApJ*, **894**, 97
- Nortmann, L., Pallé, E., Salz, M., et al. 2018, *Sci*, **362**, 1388
- Oklopčić, A. 2019, *ApJ*, **881**, 133
- Oklopčić, A., & Hirata, C. M. 2018, *ApJL*, **855**, L11
- Orell-Miquel, J., Murgas, F., Pallé, E., et al. 2022, *A&A*, **659**, A55
- Owen, J. E., & Wu, Y. 2017, *ApJ*, **847**, 29
- Paragas, K., Vissapragada, S., Knutson, H. A., & Oklopčić, A. 2021, AAS Meeting Abstracts 237, **543.05**
- Petigura, E. A., Rogers, J. G., Isaacson, H., et al. 2022, *AJ*, **163**, 179
- Salz, M., Czesla, S., Schneider, P. C., et al. 2018, *A&A*, **620**, A97
- Seager, S., & Sasselov, D. D. 2000, *ApJ*, **537**, 916
- Spake, J. J., Oklopčić, A., & Hillenbrand, L. A. 2021, *AJ*, **162**, 284
- Spake, J. J., Sing, D. K., Evans, T. M., et al. 2018, *Natur*, **557**, 68
- Stassun, K. G., Collins, K. A., & Gaudi, B. S. 2017, *AJ*, **153**, 136
- Szabó, G. M., & Kiss, L. L. 2011, *ApJL*, **727**, L44
- Vidal-Madjar, A., Lecavelier des Etangs, A., Désert, J. M., et al. 2003, *Natur*, **422**, 143
- Vissapragada, S., Knutson, H. A., Jovanovic, N., et al. 2020, *AJ*, **159**, 278
- Vissapragada, S., Stefánsson, G., Greklek-McKeon, M., et al. 2021, *AJ*, **162**, 222
- Wang, L., & Dai, F. 2021a, *ApJ*, **914**, 99
- Wang, L., & Dai, F. 2021b, *ApJ*, **914**, 98
- Zhang, M., Knutson, H. A., Dai, F., et al. 2023, *AJ*, **165**, 62
- Zhang, M., Knutson, H. A., Wang, L., Dai, F., & Barragán, O. 2022, *AJ*, **163**, 67